Invited Paper

Terahertz spectroscopy study of carrier dynamics and transient photoconductivity in CdSSe nanobelts

Hongwei Liu [1, 2, #], Junpeng Lu [1, #], Minrui Zheng [1], Sing Hai Tang [1], Chorng Haur Sow [1*], and Xinhai Zhang [3*]
[1] Department of Physics, 2 Science Drive 3, National University of Singapore, Singapore 117542
[2] Institute of Materials Research and Engineering, A*STAR (Agency for Science, Technology and Research), 3 Research Link, Singapore 117602
[3] Department of Electrical and Electronic Engineering, South University of Science and Technology of China, 1088 Xueyuan Road, Xili, Nanshan District, Shenzhen, Guangdong, China 518055
[#] These authors make equal contribution to this work.
[*1] Email: physowch@nus.edu.sg, [*3] Email: zhang.xh@sustc.edu.cn

(Received November 29, 2013)

Abstract: We employ terahertz spectroscopy to investigate the carrier dynamics and transient photoconductivity in ternary CdS_xSe_{1-x} nanobelts. The photocarrier density and mobility are extracted by fitting the measured frequency-dependent complex photoconductivities with the Drude-Smith model. Surprisingly, ternary CdS_xSe_{1-x} nanobelts are found to exhibit higher photoconductivity than binary CdS and CdSe. This is attributed to higher photocarrier density in ternary compound. In addition, presence of Se in the samples results in prominent CdSe-like TO phonon mode due to electron-phonon interaction. The strength of this mode shows a large drop upon photoexcitation but recovers gradually with time. These results demonstrated that growth of ternary nanostructures can be utilized to alleviate the effects of high surface defects in nanostructures and improve their photoconductivity.

Keywords: Optical pump-THz probe Spectroscopy, CdS_xSe_{1-x} nanobelts, Photoconductivity

doi: 10.11906/TST.234-248.2013.12.17

1. Introduction

In order to realize optoelectronic devices with technologically useful performance, intensive efforts are being directed towards a thorough understanding of the photoconductivity and charge transport properties of semiconductor nanostructures. In particular, 1D semiconductor nanomaterials such as nanowires and nanobelts show promise in optoelectronics, photovoltaics, chemical and biological sensing [1-9]. Photoconductivity measurement in nanostructures, however, is a challenging problem due to the inherent difficulty in fabricating electrodes onto nanometer-scaled objects. Currently, many reports on the probing of photoconductivity of nanowires/belts employed expensive and complex lithography methods to fabricate contact electrodes on the nanowires [10-14]. Naturally, the observed photoresponse of their samples depends on the interplay of the intrinsic response of nanobelts, nanobelts−nanobelts and nanobelts−electrodes contact barriers [11]. Given the wide diversity of contributing factors to the experimentally obtained results in a typical contact-based photoconductivity experiment, interpretation of the observed phenomena would be challenging. The photoresponse of nanobelts is a complex process attributable to incident light absorption, photocarrier generation, transportation trapping, detrapping and recombination processes [3, 14-16]. Therefore, charge carrier dynamics in semiconductors plays an important role in efficient charge separation and transport [17]. A further insight into charge carrier dynamics would facilitate a thorough understanding of photoconductivity property in nanobelts. To answer this challenge, optical pump-terahertz probe spectroscopy (OPTP) is an excellent approach to study the carrier dynamics on subpicosecond to nanosecond time scales [18]. Moreover, it is a noncontact electrical probe technique capable of measuring the photoconductivity of nanoscaled semiconductors without the cumbersome process of making contacts [19]. Here, we employ OPTP to study the photoconductivity of ternary CdS_xSe_{1-x} nanobelts with various compositions ($0 \leq x \leq 1$). The results demonstrate ternary compounds exhibit much enhanced photoelectronic properties in comparison to their binary counterparts (CdS and CdSe). To probe carrier dynamics in nanobelts, the excited states were photogenerated *via* a pulse from a femtosecond laser, while the complex photoconductivity can be extracted from a delayed single pulse of THz radiation. The broad bandwidth of THz waves enables the characterization of complex photoconductivity of samples covering a frequency range comparable to momentum scattering rate and typical plasma frequencies in semiconductors [20]. Recent studies about nanomaterials using terahertz spectroscopy have investigated silicon nanocrystals [21-23], InN nanorods [24], GaAs quantum well [25] and nanowires [18], CdSe and InP nanoparticles [17, 26], Graphene [27-30] and ZnO nanostructures [31].

Despite of the abundant research activities carried out on nanostructures and the demonstration of their great potentials in optoelectronic applications, high surface defect density with reduced dimensionality has always been a big drawback in optoelectronic applications. Such defects will lower the luminous efficiency and photoconductivity. Interestingly, we demonstrate here the formation of ternary alloys is an effective approach to reduce the surface defect density in nanostructures, thereby improving their photoconductivity and promoting the corresponding applications in optoelectronics. The ternary CdS_xSe_{1-x} nanobelts employed in this study are ternary II-VI compound semiconductor. These nanobelts have attracted great attention due to the widely-modulated band gap from 1.73 *eV* to 2.44 *eV* and their corresponding tunable optical properties [32]. CdS_xSe_{1-x} nanobelts have been used as the main component of nano scaled lasers [33, 34], waveguides [35] and field-effect transistors [32]. Despite the fact that most of the applications are based on the photoelectrical response of the CdS_xSe_{1-x} nanobelts, to the best of our knowledge, a systematic and clear understanding of the photoconductivity in these nanobelts is absent so far. Therefore, the aim of this work is to investigate the composition dependent photoconductivity in ternary CdS_xSe_{1-x} nanobelts. The photoconductivity is affected obviously by the composition and enhanced greatly by formation of ternary alloys. The observed higher photoconductivity in ternary alloys in comparison to their binary counterparts CdS and CdSe is attributed to the reduction of surface trapping of photocarriers, which will facilitate higher photo-carrier densities in ternary compounds. However, for the non-excited states, i.e. when the nanobelts are not illuminated by light, CdS nanobelts show the highest conductivity and carrier density. These results indicate the high responsivity of ternary CdS_xSe_{1-x} nanobelts to light and demonstrate their promising potential as photoelectric devices. In addition, the corresponding free carrier mobility of ternary CdS_xSe_{1-x} is lower than that of binary CdS and CdSe nanobelts, which is ascribed to the higher structural-defect density as revealed by the biexponential time-dependence carrier dynamics [36]. Furthermore, the CdSe- like TO mode is demonstrated in the spectrum. The variation in the interaction of electron-lattice vibration with composition is investigated based on this mode. All the results indicate that the formation of ternary alloys in nanostructures can be employed to overcome the high surface defect density and block the fast decay of the free carrier on surface, thus producing a higher photoconductivity.

2. Experimental methods

The CdS, CdSe and CdS_xSe_{1-x} nanobelts were synthesized on C-plane sapphire substrates via a conventional chemical vapor deposition method with a specially designed substrate holder for the formation of CdS_xSe_{1-x} nanobelts with high uniform stoichiometry according to our previous publications [32, 37].

The morphology, crystalline structure and component mole fraction of the nanobelts were characterized with a JEOL JSM-7600 *F* field emission scanning microscope (FESEM), JEM-2010 *F* high resolution transmission electron microscope (HETEM), X’ PERT MPD X-ray diffractometer (XRD) with Cu-Kα (1.5406 *Å*) radiation and an energy-dispersive spectroscopy (EDX).

Ultrafast pump light beam was generated with a Ti: sapphire regenerative amplifier laser system, which provides ~ 35 *fs* pulses with a center wavelength of 800 *nm* at a repetition rate of 1000 *Hz*. The fundamental output was frequency doubled via a 1 *mm* thick β-barium borate (BBO) crystal to generate excitation pulses with a wavelength of 400 *nm*. The THz probe beam with spectrum range from 0.3 to 5 *THz* was generated with air-plasma technique [38] and detected by a THz Air-Biased-Coherent-Detection (THz-ABCD) method [39, 40]. The samples were excited at 45 degree incidence while the THz wave passed through the samples at normal incidence. All the measurements were carried out in a dry nitrogen purge environment at room temperature.

3. Results and discussions

In this study, we examine CdS_xSe_{1-x} nanobelts grown on C-plane sapphire substrate. The top view and side view of SEM images and a HRTEM image of a representative sample are shown in Figure 1(a). The belt-like morphology with a uniform thickness of about 30 *nm*, 100-200 *nm* in width and an average length of about several tens of micrometers is shown. Revealed by the HRTEM image, the nanobelt possesses high quality crystallinity. Figure 1(b) shows the XRD patterns of five CdS_xSe_{1-x} samples with different compositions (x = 0, 0.29, 0.65, 0.87, and 1, respectively). All the nanobelts exhibit high purity wurtzite structure without impurity phases. We calculate the composition and lattice constant of each sample by Vegard's law from the (100) or (002) peak. The calculated x values are consistent with the values obtained from EDX spectra displayed in Figure 1(c). The corresponding normalized PL spectra of these samples are plotted in Figure 1(d). All of the nanobelts exhibit near-band-edge emission peak with narrow line-width and the peak positions gradually red-shift from 507 *nm* (CdS) to 713 *nm* (CdSe) with decreasing x.

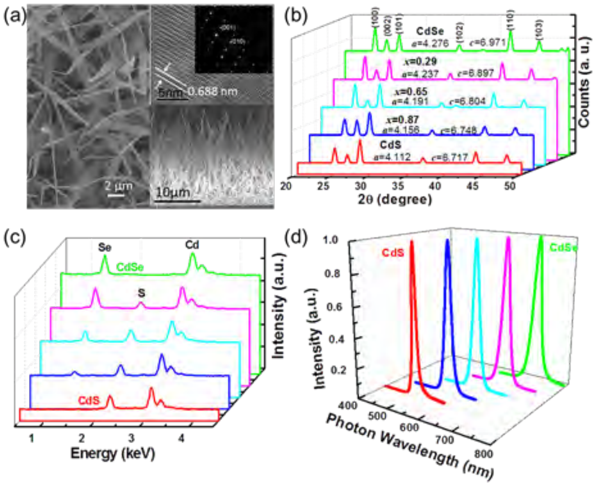

Fig. 1 (a) SEM and HRTEM images of a representative CdS_xSe_{1-x} sample. (b) XRD patterns, (c) EDX spectra, and (d) PL spectra of five different CdS_xSe_{1-x} samples with x = 0, 0.29, 0.65, 0.87, and 1, respectively.

Composition dependent carrier dynamics of CdS_xSe_{1-x} nanobelts are investigated from OPTP pump scans and the composition dependent conductivity are obtained from OPTP probe scans [17, 19, 41]. In the pump scan, the transient behavior of the photoexcited carriers can be monitored by tracing the differential transmission $\Delta T / T_0$ of THz waveforms at the peak amplitude as a function of delay time between the optical pump pulse and THz probe pulse. Here T_0 is the transmitted intensity of THz pulses passing through the sample without optical excitation, and ΔT is the time-dependent transmission change of THz wave resulted from optical excitation. Figure 2 shows the OPTP pump scan signals of a variety of CdS_xSe_{1-x} nanobelts with different composition. All samples were excited by 400 *nm* laser at the excitation fluence of 40, 20, 10, and 5 $\mu J/cm^2$. THz transmission ($\Delta T / T_0$) of all samples instantaneously drop as the pump pulse arrives. Despite of the different compositions, similar sharp fall times of 3.5-3.8 *ps* are measured. However, for the decay process, different decay times are observed for samples with different compositions. The experimental data are well-fitted by a biexponential function (solid lines in Figure 2(a)-(e)),

$$\Delta T / T_0 = A_1 e^{-t/\tau_1} + A_2 e^{-t/\tau_2} \tag{1}$$

where A_i is the weighting factor and τ_i is relaxation time constant. The function corresponds to a rapid process (with small τ_1) and a slower response (with large τ_2). Figure 2(f) plots the best fit parameters (based on the 40 $\mu J/cm^2$ excitation fluence data) of the five samples with different

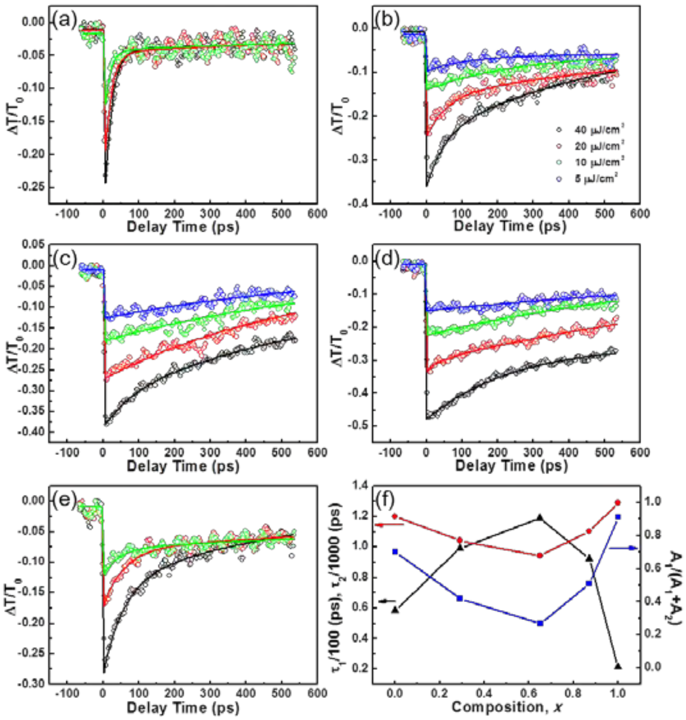

Fig. 2 Time-dependent differential terahertz transmission $\Delta T / T_0$ of (a) CdS, (b) $CdS_{0.87}Se_{0.13}$, (c) $CdS_{0.65}Se_{0.35}$, (d) $CdS_{0.29}Se_{0.71}$ (e) CdSe. All transients are well fitted by a biexponential function. (f) Extracted parameters: ▲ = $\tau_1/100$; ● =$\tau_2/1000$; ■ = $A_1/(A_1+A_2)$ plotted as a function of x value based on the 40 $\mu J/cm^2$ excitation fluence data.

composition as a function of x value. Evidently, the binary compound CdS and CdSe nanobelts exhibit smaller decay time τ_1 and larger τ_2. On the contrary, the ternary CdS_xSe_{1-x} nanobelts show larger τ_1 than binary compound and smaller τ_2. As the x value increases to 0.65, the nanobelt shows the largest decay time τ_1 and smallest decay time τ_2. This implies the fast process becomes slower when the S- and Se- compositions are comparable in the ternary nanobelts. As revealed by the weighting factor $A_1/(A_1+A_2)$, the binary nanobelts have higher ratio values (> 50%) than those of ternary CdS_xSe_{1-x} nanoebtls (< 50%). This indicates the fast process dominates the free carrier decay in binary nanobelts whilst the slow process is the more preferred decay channel in the ternary alloys.

As demonstrated in our previous report [36], the biexponential relaxation is due to the rapid carriers capture by surface defects and slow band-to-band transition in CdS and CdSe nanobelts. As revealed by the low-temperature PL studies, binary CdS and CdSe nanobelts possess higher surface defect density states than that of ternary CdS_xSe_{1-x} nanobelts [42]. Hence the rapid surface trapping is expected to be the dominant decay path in the whole relaxation process of binary nanobelts. In ternary alloys, the slow decay process corresponds to structured defects related recombinations. The structural-defects are attributed to compositional fluctuations and structural anomalies, in which the two bond lengths in the ternary alloy maintain two chemically distinct values. When S- and Se- compositions become comparable ($x = 0.5$), the structural-defect density is expected to be maximum. Therefore, $CdS_{0.65}Se_{0.35}$ shows the smallest τ_2 among our samples.

In the OPTP probe scan collection, the spectra are obtained by monitoring the entire THz pulse transmission at a given pump-probe delay time. A fast Fourier transform is then applied on the time-domain waveform to obtain frequency domain spectra. The spectra include a great deal of information about the conduction mechanism. From the transmitted THz pulse electric field $\tilde{E}_{sam}(\omega)$ passing through sample and reference electric field $\tilde{E}_{ref}(\omega)$ passing through substrate, the complex transmission $\tilde{t}(\omega)$ is given by [43],

$$\tilde{t}(\omega) = \frac{\tilde{E}_{sam}(\omega)}{\tilde{E}_{ref}(\omega)} = \frac{\dfrac{t_{12}t_{23}\exp[i(n_2+ik_2)\omega d/c]}{1-r_{21}r_{23}\exp[i2(n_2+ik_2)\omega d/c]}}{t_{13}\exp(in_1\omega d/c)} \approx 1+\frac{i\omega d}{c}\left[\frac{(n_2+ik_2)^2-n_1^2}{n_1+n_3}\right] \tag{2}$$

where 1, 2 and 3 denote nitrogen, sample and substrate respectively. t_{ij} and r_{ij} are transmission and reflection coefficients of $i \rightarrow j$ interface (i, j=1, 2, 3 and $i \neq j$). n is refractive index, c is speed of light, d is thickness of sample (measured from SEM images) and ω is the radial frequency.

The complex refractive index $\tilde{n}(\omega) = n_2 + ik_2$ can be determined from Eq. (2), and then the conductivity can be estimated using the following relationships,

$$\tilde{\varepsilon}(\omega) = \varepsilon_\infty + i\tilde{\sigma}(\omega)/\omega\varepsilon_0 = (n+ik)^2 \tag{3}$$

where $\tilde{\varepsilon}(\omega)$ and $\tilde{\sigma}(\omega)$ are complex dielectric function and complex conductivity. ε_∞ is high-frequency constant of the material and ε_0 is free space permittivity. To obtain the conductivity of pure nanobelts, an effective medium approximation [44, 45], $\varepsilon_{eff}(\omega) = f\varepsilon_{sample}(\omega) + (1-f)\varepsilon_{N_2}$, is employed, where ε_{N_2} = 1.00058 at room temperature, and f is the filling factor. Figure 3 shows the measured complex conductivities of six samples with different composition (x=1, 0.87, 0.75, 0.65, 0.29 and 0, respectively) at equilibrium state. Evidently, the real part of the conductivity, Re[σ] of CdS (Figure 3(a)) increases with increasing frequency, while its imaginary part Im[σ] decreases. Interestingly, with the appearance of "Se" in samples, a resonance oscillator peak appears at around 5 *THz* and becomes prominent and the strength of the oscillator enhances with increasing "Se" concentration. When the THz wave propagates through a sample, the electric field not only interacts with free carriers, but also couples with the optical phonons in material, and thus different dielectric responses appear in spectrum. Compared with our previously reported CdS_xSe_{1-x} Raman spectra [32], this oscillator is attributed to CdSe- like transverse optical (TO) mode. We employ the Drude-Smith model combined a damped oscillator to represent the carrier conductivity in the nanobelts, in which the complex conductivity function is described by [46]

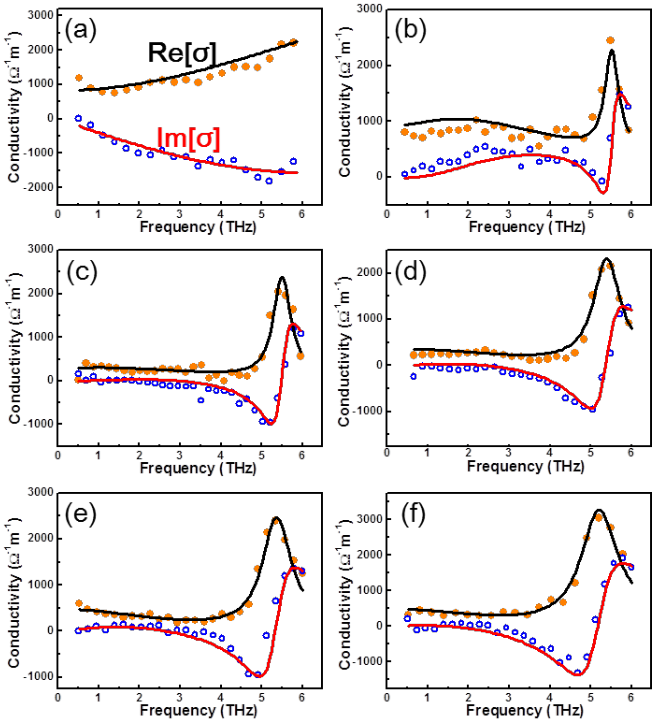

Fig. 3 Measured frequency-dependent complex conductivities of six samples with different composition (x = (a) 1, (b) 0.87, (c) 0.75, (d) 0.65, (e) 0.29 and (f) 0, respectively) and solid lines show the fitted data by Drude-Smith model.

$$\sigma(\omega)=\frac{\varepsilon_0\tau_0\omega_p^2}{1-i\omega\tau_0}(1+\frac{c}{1-i\omega\tau_0})+\frac{i\omega\varepsilon_0 A\omega_o^2}{\omega_o^2-\omega^2-i\gamma\omega} \tag{4}$$

where $\omega_p^2 = Ne^2/(m^*\varepsilon_0)$ is the plasma frequency, in which N_o is free carrier density, e is the charge of electron and m^* is the electron effective mass. τ is the electron scattering time. A is oscillator strength, ω_o is optical phonon eigenfrequency, and γ is carrier damping constant, which defines the width of resonance. According to the best fitting, the composition phase-diagram contour maps of the real part and imaginary part of the conductivity of static state are shown in Figure 4(a) and (b), respectively. Extracted from these fitting results, the free carrier density N_o, dc conductivity σ_o, and electron mobility μ can be calculated and plotted as a function of composition x, as shown in Figure 4(c). Evidently, the free carrier density increases with increasing sulfur concentration but the electron mobility decreases monotonously with increasing x. As a result, the dc conductivity, $\sigma_o=(1+c)(eN_o\mu)$, of CdS presents a maximum dc conductivity value and $CdS_{0.75}Se_{0.25}$ shows the lowest dc conductivity value (σ_o increases with x at the beginning, and then decreases with x after x = 0.75). Meanwhile, both the amplitude (strength, A) and peak width (γ) of the CdSe- like TO phonon mode decreases linearly with decreasing "Se" composition and vanished at $x = 1$ (i.e. CdS). Moreover, the peak position gradually shifts upward from 5.24 THz (174.5 cm^{-1}, CdSe) to 5.55 THz (184.8 cm^{-1}, $CdS_{0.87}Se_{0.13}$) with decreasing Se-concentration, as shown in Figure 4(d). Similar shifting in the CdS/CdSe- like LO modes in CdS_xSe_{1-x} nanobelts was observed using Raman spectroscopy [32]. This phenomenon is attributed to alloy potential fluctuations and can be explained by a modified "random-element-isodisplacement" model [37, 47, 48].

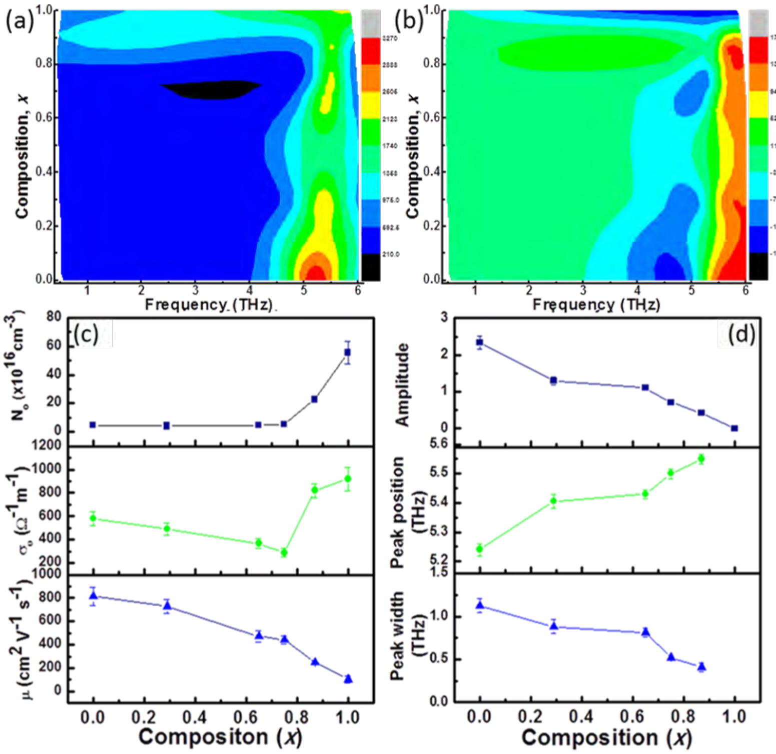

Fig. 4 Composition phase-diagram of the (a) real part and (b) imaginary part of the static conductivity. (c) Calculated free carrier density N_o, dc conductivity σ_o, and electron mobility μ and (d) CdSe- like TO mode strength, peak position and peak width of six samples plotted as a function of composition x.

Investigating the non-equilibrium state of semiconductor materials under photon excitation is essential in optimization of nano-scaled optoelectronic devices. Upon laser excitation, the THz probe scans at different delay times were performed. As a result, the transient conduction properties of CdS_xSe_{1-x} nanobelts at non-equibrium state can be investigated with time. Figure 5(a)-(d) show the complex conductivity spectra of a representative sample ($x = 0.75$) at different delay time after photoexcitation. Figure 5(a) presents the conductivity at $t = 3.5ps$, at which point the nanobelts were fully excited and $\Delta T / T_0$ shows the maximum amplitude. With increasing delay time, the free carriers were depleting and the corresponding conductivities were recorded at *t*=89, 235, and 500 *ps*, as shown in Figure 5(b), (c), and (d), respectively. Figure 5(e) shows the electron mobility as a function of time. The value recorded at 0 *ps* is the mobility of CdS_xSe_{1-x} nanobelts at static state. Evidently, the electron mobility sharply increases at the onset of laser excitation and then gradually decreases with delay time due to the free carrier trapping and localization.

The information of photoconductivity $\Delta\sigma(\omega,t)$ can be extracted from the recorded transient

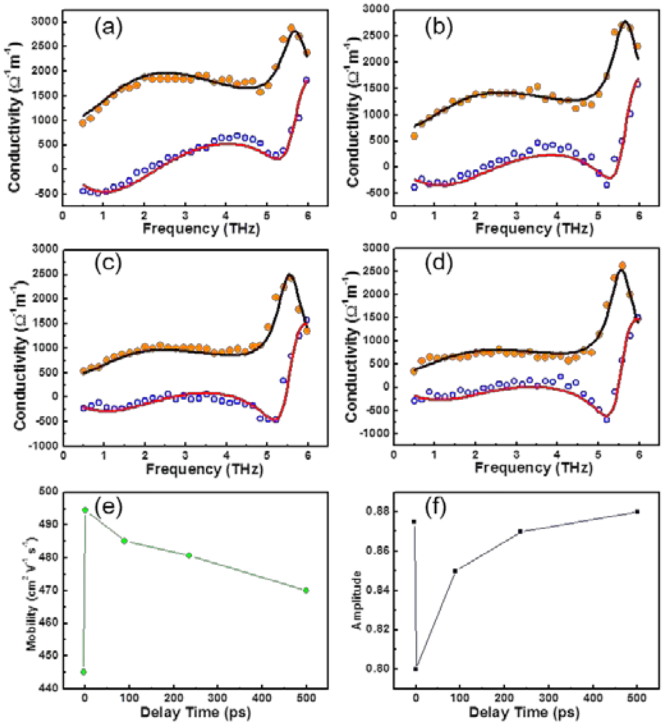

Fig. 5 Complex conductivity of a representative sample ($CdS_{0.75}Se_{0.25}$) at different delay time, (a) 3.5 *ps*, (b) 89 *ps*, (c) 235 *ps*, and (d) 500 *ps*. (e) electron mobility and (f) the strength of the CdSe- like TO mode plotted as a function of time.

change in terahertz transmission. The expression of photoconductivity is derived as,

$$\Delta\sigma(\omega,t) = -\frac{\varepsilon_0 c(n_1+n_2)}{d}\frac{\Delta\tilde{E}_{sam}(\omega,t)}{\tilde{E}_{sam}(\omega)} \tag{5}$$

where *t* is the pump-probe delay time. Figure 6 shows the photoconductivity of six samples (*x*=1, 0.87, 0.75, 0.65, 0.29 and 0, respectively) recorded at *t*=3.5 *ps*. Here, the real part of the photoconductivity (black circle) may be considered as the resistive response of the nanobelts, with the imaginary part as an additional inductive or capacitive response [18]. The real part photoconductivity (Re[Δσ]) of all nanobelts are positive but ternary CdS_xSe_{1-x} nanobelts show larger Re[Δσ] values than those of binary CdS and CdSe nanobelts, indicating that ternary nanobelts exhibit higher responsivity to light. The contour mapping of the fitting results in Figure

7(a) and (b) show the real and imaginary parts of the photoconductivity, respectively, as a function of the composition. The corresponding values of Re[Δσ] at 2 *THz* as a function of composition are plotted in Figure 7(c). As shown, CdSe nanobelts present the minimum Re[Δσ] value while $CdS_{0.75}Se_{0.25}$ show the maximum value, which is consistent with our previous photoresponse experiment with applied bias under light illumination [32]. The Re[Δσ] value can be measured as high as 900 $\Omega^{-1}cm^{-1}$, which is much higher than the photoconductivity values of III-V compound nanowires and other II-VI compound nanostructures [49-53]. To the best of our knowledge, this is the highest photoconductivity value in semiconductor nanostructures as reported using similar THz characterization techniques. The high photoconductivity in ternary CdS_xSe_{1-x} nanobelts is directly related to the high free carrier intensity in the nanobelts. The reduction of surface defect density in ternary alloys is an important aspect, due to the corresponding reduction in the free carrier trapping. Furthermore, the real part photoconductivities of CdS and CdSe do not show distinct frequency dependence, which indicates that photoinduced free carriers possess a large scattering rate in CdS and CdSe nanobelts. However, in ternary CdS_xSe_{1-x} nanobelts, a broad peak appears in the real part accompanied by a corresponding zero crossing in the imaginary part of photoconductivity (as illustrated by black and red arrows in Figure 6(b)-(e)). This feature is located at low frequency region when “S” and “Se” are comparable, and shifts to high frequency region when “S” or “Se” is rich. The appearance of this feature is attributed to excitonic transition [25]. In short, the

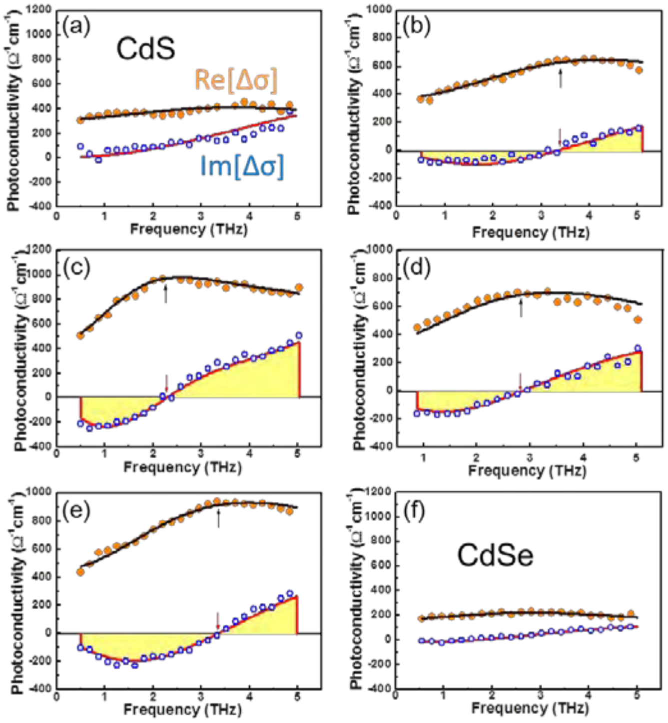

Fig. 6 Complex photoconductivity of six samples (*x* = (a) 1, (b) 0.87, (c) 0.75, (d) 0.65, (e) 0.29, and (f) 0, respectively) recorded at *t* = 3.5 *ps*. The solid lines are Drude-Smith fitting curves.

transformation of photoexcited unbound e-h pairs into excitons requires a transient phonon bath into which the momentum and binding energy can be permanently released. Due to the higher photogenerated free carrier densities (Figure 7(d)) in ternary CdS_xSe_{1-x} nanobelts, the features are revealed more obviously in ternary nanobelts spectra. The photocarrier densities are obtained from the best fitting (solid lines in Figure 6) parameters. Both the photocarrier density and the corresponding free electron mobility are plotted as a function of composition x, as shown in Figure 7(d). The higher photocarrier density of ternary CdS_xSe_{1-x} nanobelts also provides a certification for their large real part photoconductivity values. Conversely, the mobility of photocarriers in binary CdS and CdSe is higher than that in ternary CdS_xSe_{1-x} nanobelts, which

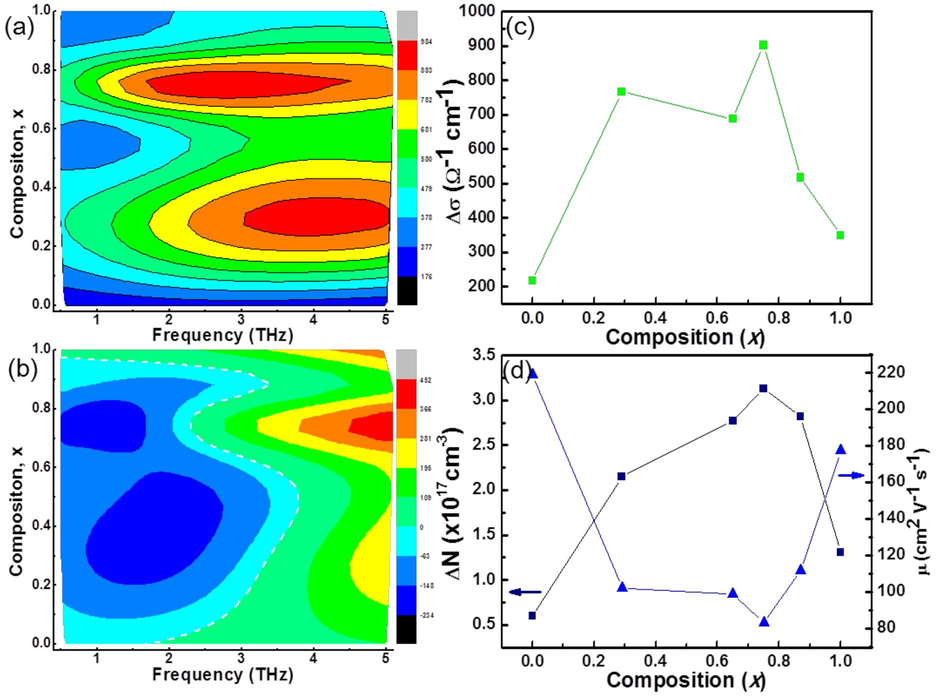

Fig. 7 (a) Real and (b) imaginary parts of the photoconductivity as a function of composition. The white dash contour in b represents Im[Δσ] = 0, corresponding to the peak frequency, ω_o. (c) Real part of photoconductivity at 2 *THz* plotted as a function of composition. (d) Photocarrier density (ΔN) and photocarrier mobility plotted as a function of composition.

presents a different relationship from that at static state before laser excitation (Figure 4(a)), in which the free carrier mobility in CdSe is higher than CdS_xSe_{1-x}. This is possibly attributed to the Anderson localization [54] or the higher chance of excition formation in CdS_xSe_{1-x} nanobelts. Despite of the comparatively lower mobility, the much higher photocarrier intensity compensates the lower mobility and provide a higher photoconductivity in ternary CdS_xSe_{1-x} nanobelts.

4. Conclusions

In summary, we have studied the carrier dynamics and transient photoconductivity in ternary CdS_xSe_{1-x} nanobelts using OPTP. The observed carrier dynamics of binary CdS and CdSe nanobelts display much shorter lifetimes than those of ternary CdS_xSe_{1-x} nanobelts, which is critically dependent on the trap density at the binary nanobelt surface. These results indicate the possibility for implementation of ultrafast switching devices using nanobelts (especially, CdS, which indicating a switching speed potentially up to 46.7 *GHz*). Conversely, the ternary CdS_xSe_{1-x} nanobelts present much higher photoconductivity than that of binary nanobelts, which is attributed to the higher photocarrier densities due to the reduced surface trapping in ternary compound. These results demonstrate the high light responsivity of ternary CdS_xSe_{1-x} nanobelts and show their promising potential as photoelectric devices such as phototransistor and solar cells. In addition, the photocarrier mobility of ternary CdS_xSe_{1-x} is lower than that of binary compound nanobelts, due to the carrier localization. Our investigation of composition-dependence photoconductivity in ternary CdS_xSe_{1-x} nanobelts will promote design, fabrication and optimization of nanobelt-based photoelectronic devices.

References

[1] B. Tian, X. Zheng, T. J. Kempa, et. al.. "Coaxial silicon nanowires as solar cells and nanoelectronic power sources". *Nature, 449*, 885-889 (2007).

[2] R. Yan, D. Gargas, P. Yang. "Nanowire photonics". *Nat. Photon., 3*, 569-576 (2009).

[3] L. Cao, J. S. White, J.-S. Park, et. al.. "Engineering light absorption in semiconductor nanowire devices". *Nat Mater, 8*, 643-647 (2009).

[4] T. Dietl and H. Ohno. "Engineering magnetism in semiconductors". *Mater. Today, 9*, 18-26 (2006).

[5] J. Wang, M. S. Gudiksen, X. Duan, et. al.. "Highly Polarized Photoluminescence and Photodetection from Single Indium Phosphide Nanowires". *Science, 293*, 1455-1457 (2001).

[6] M. D. Kelzenberg, D. B. Turner-Evans, B. M. Kayes, et. al.. "Photovoltaic Measurements in Single-Nanowire Silicon Solar Cells". *Nano Lett., 8*, 710-714 (2008).

[7] Y. Cui, Q. Wei, H. Park, et. al.. "Nanowire Nanosensors for Highly Sensitive and Selective Detection of Biological and Chemical Species". *Science, 293*, 1289-1292 (2001).

[8] Y. H. Ahn, J. Park. "Efficient visible light detection using individual germanium nanowire field effect transistors". *Appl. Phys. Lett., 91*, 162102-3 (2007).

[9] Q. H. Li, Y. X. Liang, Q. Wan, et. al.. "Oxygen sensing characteristics of individual ZnO nanowire transistors". *Appl. Phys. Lett., 85*, 6389-6391 (2004).

[10] Z.-M. Liao, Y. Lu, J. Xu, et. al.. "Temperature dependence of photoconductivity and persistent photoconductivity of single ZnO nanowires". *Applied Physics A: Materials Science & Processing, 95*, 363-366 (2009).

[11] T. Rajesh, V. Binni, G. M. Subodh, et. al.. "Probing the photoresponse of individual Nb 2 O 5 nanowires with

global and localized laser beam irradiation". *Nanotechnology, 22*, 115202 (2011).

[12] T. Zhai, X. Fang, M. Liao, et. al.. "A Comprehensive Review of One-Dimensional Metal-Oxide Nanostructure Photodetectors". *Sensors, 9*, 6504-6529 (2009).

[13] S. P. Mondal, and S. K. Ray. "Enhanced broadband photoresponse of Ge/CdS nanowire radial heterostructures". *Appl. Phys. Lett., 94*, 223119-3 (2009).

[14] C. Soci, A. Zhang, B. Xiang, et. al.. "ZnO Nanowire UV Photodetectors with High Internal Gain". *Nano Lett., 7*, 1003-1009 (2007).

[15] S. Thunich, L. Prechtel, D. Spirkoska, et. al.. "Photocurrent and photoconductance properties of a GaAs nanowire". *Appl. Phys. Lett., 95*, 083111-3 (2009).

[16] H. Pettersson, J. Trägårdh, A. I. Persson, et. al.. "Infrared Photodetectors in Heterostructure Nanowires". *Nano Lett., 6*, 229-232 (2006).

[17] M. C. Beard, G. M. Turner, and C. A. Schmuttenmaer. "Size-Dependent Photoconductivity in CdSe Nanoparticles as Measured by Time-Resolved Terahertz Spectroscopy". *Nano Lett., 2*, 983-987 (2002).

[18] P. Parkinson, J. Lloyd-Hughes, Q. Gao, et. al.. "Transient Terahertz Conductivity of GaAs Nanowires". *Nano Lett., 7*, 2162-2165 (2007).

[19] M. C. Beard, G. M. Turner, and C. A. Schmuttenmaer. "Transient photoconductivity in GaAs as measured by time-resolved terahertz spectroscopy". *Phys. Rev. B, 62*, 15764-15777 (2000).

[20] C. A. Schmuttenmaer. "Exploring Dynamics in the Far-Infrared with Terahertz Spectroscopy". *Chem. Rev., 104*, 1759-1780 (2004).

[21] H.-K. Nienhuys, and V. Sundstrom. "Influence of plasmons on terahertz conductivity measurements". *Appl. Phys. Lett., 87*, 012101-3 (2005).

[22] P. U. Jepsen, W. Schairer, I. H. Libon, et. al.. "Ultrafast carrier trapping in microcrystalline silicon observed in optical pump--terahertz probe measurements". *Appl. Phys. Lett., 79*, 1291-1293 (2001).

[23] D. G. Cooke, A. N. MacDonald, A. Hryciw, et. al.. "Transient terahertz conductivity in photoexcited silicon nanocrystal films". *Phys. Rev. B, 73*, 193311 (2006).

[24] H. Ahn, Y. P. Ku, Y. C. Wang, et. al.. "Terahertz spectroscopic study of vertically aligned InN nanorods". *Appl. Phys. Lett., 91*, 163105-3 (2007).

[25] R. A. Kaindl, M. A. Carnahan, D. Hagele, et. al.. "Ultrafast terahertz probes of transient conducting and insulating phases in an electron-hole gas". *Nature, 423*, 734-738 (2003).

[26] M. C. Beard, G. M. Turner, J. E. Murphy, et. al.. "Electronic Coupling in InP Nanoparticle Arrays". *Nano Lett., 3*, 1695-1699 (2003).

[27] P. A. George, J. Strait, J. Dawlaty, et. al.. "Ultrafast Optical-Pump Terahertz-Probe Spectroscopy of the Carrier Relaxation and Recombination Dynamics in Epitaxial Graphene". *Nano Lett., 8*, 4248-4251 (2008).

[28] J. H. Strait, H. Wang, S. Shivaraman, et. al.. "Very Slow Cooling Dynamics of Photoexcited Carriers in Graphene Observed by Optical-Pump Terahertz-Probe Spectroscopy". *Nano Lett., 11*, 4902-4906 (2011).

[29] G. Jnawali, Y. Rao, H. Yan, et. al.. "Observation of a Transient Decrease in Terahertz Conductivity of Single-Layer Graphene Induced by Ultrafast Optical Excitation". *Nano Lett., 13*, 524-530 (2013).

[30] C. J. Docherty, C.-T. Lin, H. J. Joyce, et. al.. "Extreme sensitivity of graphene photoconductivity to environmental gases". *Nat. Commun., 3*, 1228 (2012).

[31] J. B. Baxter, and C. A. Schmuttenmaer. "Conductivity of ZnO Nanowires, Nanoparticles, and Thin Films Using Time-Resolved Terahertz Spectroscopy†". *J. Phys. Chem. B, 110*, 25229-25239 (2006).

[32] J. Lu, C. Sun, M. Zheng, et. al.. "Facile One-Step Synthesis of CdSxSe1–xNanobelts with Uniform and Controllable Stoichiometry". *J. Phys. Chem. C, 115*, 19538-19545 (2011).

[33] A. Pan, W. Zhou, E. S. P. Leong, et. al.. "Continuous Alloy-Composition Spatial Grading and Superbroad Wavelength-Tunable Nanowire Lasers on a Single Chip". *Nano Lett., 9*, 784-788 (2009).

[34] G. Li, Y. Jiang, Y. Wang, et. al.. "Synthesis of CdSXSe1−X Nanoribbons with Uniform and Controllable Compositions via Sulfurization: Optical and Electronic Properties Studies". *J. Phys. Chem. C, 113*, 17183-17188 (2009).

[35] A. Pan, X. Wang, P. He, et. al.. "Color-Changeable Optical Transport through Se-Doped CdS 1D Nanostructures". *Nano Lett., 7*, 2970-2975 (2007).

[36] H. Liu, J. Lu, H. F. Teoh, et. al.. "Defect Engineering in CdSxSe1–x Nanobelts: An Insight into Carrier Relaxation Dynamics via Optical Pump–Terahertz Probe Spectroscopy". *J. Phys. Chem. C, 116*, 26036-26042 (2012).

[37] J. Lu, H. Liu, C. Sun, et. al.. "Optical and electrical applications of ZnS(x)Se(1-x) nanowires-network with uniform and controllable stoichiometry". *Nanoscale, 4*, 976-81 (2012).

[38] X. Xie, J. Dai, and X. C. Zhang. "Coherent Control of THz Wave Generation in Ambient Air". *Phys. Rev. Lett., 96* (2006).

[39] N. Karpowicz, J. Dai, X. Lu, et. al.. "Coherent heterodyne time-domain spectrometry covering the entire “terahertz gap”". *Appl. Phys. Lett., 92*, 011131 (2008).

[40] J. Lu, H. Liu, S. X. Lim, et. al.. "Transient Photoconductivity of Ternary CdSSe Nanobelts As Measured by Time-Resolved Terahertz Spectroscopy". *J. Phys. Chem. C, 117*, 12379-12384 (2013).

[41] M. C. Beard, G. M. Turner, and C. A. Schmuttenmaer. "Subpicosecond carrier dynamics in low-temperature grown GaAs as measured by time-resolved terahertz spectroscopy". *J. Appl. Phys., 90*, 5915-5923 (2001).

[42] H. W. Liu, J. P. Lu, H. M. Fan, et. al.. "Temperature and composition dependence of photoluminescence dynamics in CdS[sub x]Se[sub 1 - x] (0 <= x <= 1) nanobelts". *J. Appl. Phys., 111*, 073112-6 (2012).

[43] T.-R. Tsai, S.-J. Chen, C.-F. Chang, et. al.. "Terahertz response of GaN thin films". *Opt. Express, 14*, 4898-4907 (2006).

[44] F. J. García-Vidal, J. M. Pitarke, and J. B. Pendry. "Effective Medium Theory of the Optical Properties of Aligned Carbon Nanotubes". *Phys. Rev. Lett., 78*, 4289-4292 (1997).

[45] H. C. Weissker, J. Furthmüller, and F. Bechstedt. "Validity of effective-medium theory for optical properties of embedded nanocrystallites from ab initio supercell calculations". *Phys. Rev. B, 67*, 165322 (2003).

[46] Valeri P. Tolstoy, Irina V. Chernyshova, V. A. Skryshevsky, *Handbook of Infrared Spectroscopy of Ultrathin Films*. John Wiley & Sons, Inc: USA (2003).

[47] P. Parayanthal, and F. H. Pollak. "Raman Scattering in Alloy Semiconductors: "Spatial Correlation" Model". *Phys. Rev. Lett., 52*, 1822-1825 (1984).

[48] I. F. Chang, and S. S. Mitra. "Application of a Modified Random-Element-Isodisplacement Model to Long-Wavelength Optic Phonons of Mixed Crystals". *Phys. Rev., 172*, 924-933 (1968).

[49] C. K. Yong, K. Noori, Q. Gao, et. al.. "Strong Carrier Lifetime Enhancement in GaAs Nanowires Coated with Semiconducting Polymer". *Nano Lett., 12*, 6293-6301 (2012).

[50] H. J. Joyce, J. Wong-Leung, C.-K. Yong, et. al.. "Ultralow Surface Recombination Velocity in InP Nanowires Probed by Terahertz Spectroscopy". *Nano Lett., 12*, 5325-5330 (2012).

[51] P. Parkinson, C. Dodson, H. J. Joyce, et. al.. "Noncontact Measurement of Charge Carrier Lifetime and Mobility in GaN Nanowires". *Nano Lett., 12*, 4600-4604 (2012).

[52] H. J. Joyce, Q. Gao, H. Hoe Tan, et. al.. "III–V semiconductor nanowires for optoelectronic device applications". *Prog. Quant. Electron., 35*, 23-75 (2011).

[53] J. B. Baxter, and C. A. Schmuttenmaer. "Carrier dynamics in bulk ZnO. II. Transient photoconductivity measured by time-resolved terahertz spectroscopy". *Phys. Rev. B, 80*, 235206 (2009).

[54] P. W. Anderson. "Absence of Diffusion in Certain Random Lattices". *Phys. Rev., 109*, 1492-1505 (1958).